Supplementary Material

1 OBSERVATIONAL DATA AND METHODS

1.1 Field site

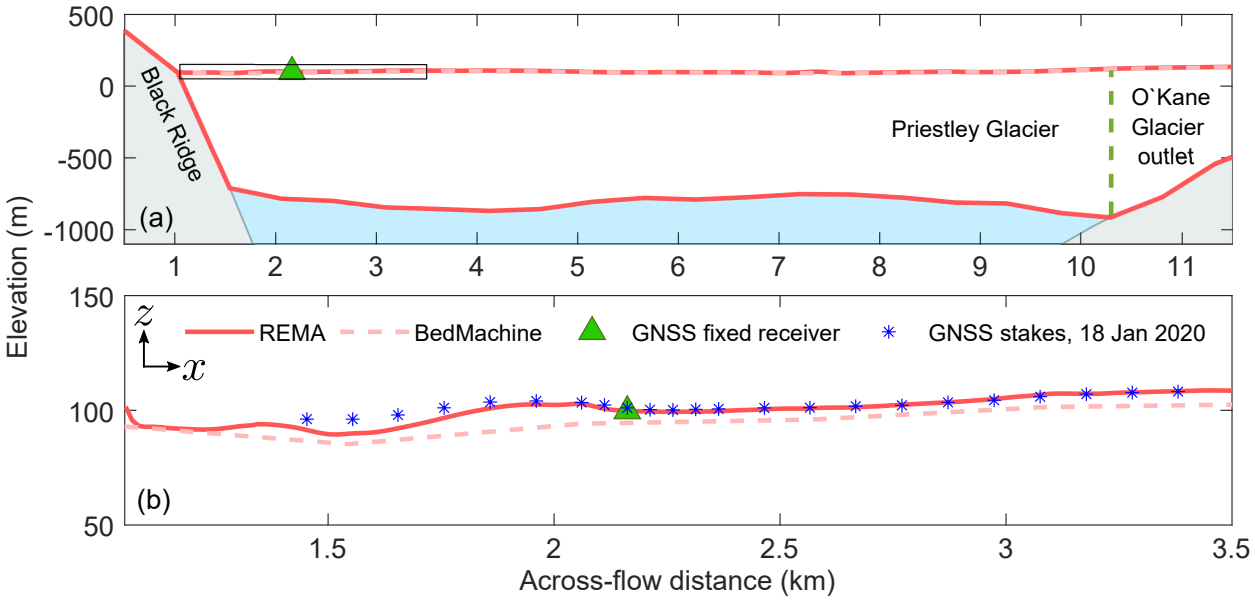

Figure S1. (a) The geometry of the across-flow profile intersecting the field site. Ice thickness and surface elevation are from the BedMachine Version 2 compilation (Morlighem et al., 2020). (b) The ice surface elevation across Priestley Glacier's shear margin. The BedMachine compilation includes the ice surface elevation (from the Reference Elevation Model of Antarctica, REMA) and thickness at a 500 m grid-spacing, while the REMA has a 10 m grid spacing (Howat et al., 2019; Morlighem et al., 2020). Blue stars indicate the locations of glacier stakes installed across the shear margin.

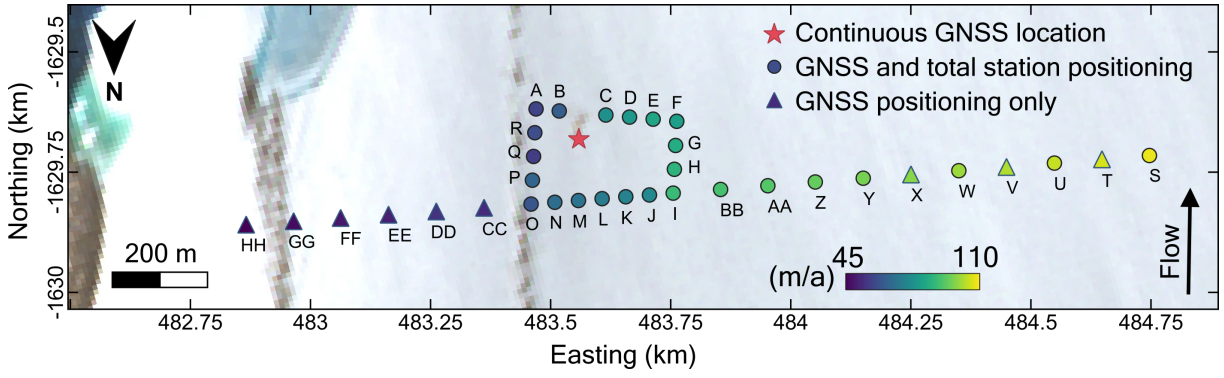

Figure S2. Locations of glacier stakes installed across Priestley Glacier's shear margin. The basemap is a Sentinel-2, 10 m true colour composite image, acquisition date 17 January, 2020, courtesy of the European Space Agency.

1.2 GNSS data

Two Trimble R10 dual-frequency GNSS receivers were used for the Priestley Glacier fieldwork. The first receiver was fixed to the glacier surface and provided a continuous record of tidally-modulated ice position (1 to 18 January, 2020) and a second roving receiver was used to observe the positions of an array of glacier stakes installed across the shear margin (Figs. S1, S2). The raw GNSS data collected by both receivers is post-processed using Trimble Business Center software (Version 5.4). The correction of the glacier GNSS occupations uses the reference station at Jang Bogo (Trimble NetR9, GPS + Galileo observations only, 30 km baseline). This reference station operated for the entirety of the field campaign at a sampling interval of 1 second. Broadcast ephemeris data were downloaded from the International GNSS Service (IGS). This correction provides post-processed kinematic solutions using the GPS and Galileo satellite systems (25+ satellites). Measurement precision (1σ) is 0.5 cm (easting), 1.3 cm (northing) and 2.5 cm (vertical) (n = 500 consecutive measurements collected over 2 hours).

1.2.1 Continuous GNSS record of ice motion

Further adjustments are made to the processed 18-day GNSS time series to facilitate the present study. The coordinate system axes are rotated from the WGS 84/Antarctic Polar Stereographic coordinate system to a flow-following coordinate system with horizontal x and y axes orientated in the across-flow and along-flow directions, respectively. A ∼2-day section of the record is translated downstream by 3 cm to correct for a slip of the GNSS receiver tripod. High frequency noise in the GNSS time series is reduced using a simple moving average (Fig. 2). Ice velocity components v_x, v_y and v_z are computed as the slope of a linear regression between time and the horizontal displacement components, using a moving window. Window size affects maximum amplitude and noise in the resulting velocity record and a 6-hour window is used here.

1.2.2 GNSS–derived stake velocities

Along- and across-flow velocity components, v_x, v_y, are computed for each glacier stake in Fig. S2 as the slope of the best linear least-squares fit for the displacement in the two directions, Δx and Δy, as a function of time t (Table S1). Uncertainty in the velocity components is computed following error propagation theory (Taylor, 1997, p.g., 181). If the mean velocity $\bar{v}$ is the slope of the displacement as a function of time ($\Delta x/\Delta t$), an estimate of the uncertainty σ_x in the observed stake displacements is

$$\sigma_x = \sqrt{\frac{1}{N-2}\sum_{i=1}^{N}(x_i - A - Bt_i)^2} \tag{S1}$$

where N is the number of measured stake positions, and A and B are the constants of the least-squares fit line $y = A + Bx$. The uncertainty in the slope σ_B (i.e., the uncertainty in the mean stake velocity) is

$$\sigma_B = \sigma_x\sqrt{\frac{N}{\Delta}} \tag{S2}$$

where $\Delta = N\sum t^2 - (\sum t)^2$. We assume that the uncertainty in the time observation is negligible and the uncertainties in the position observations have the same magnitude.

Table S1. Ice velocities determined via GNSS positioning. $\boldsymbol{v}$ is the average ice velocity computed as a least squares best fit line between position and time. The bearing is the line of best fit through all measured stake positions. Stakes HH through to S form a transect across the shear margin, while stakes A to R form a loop around a shallow ice coring site. n is the number of GNSS observations obtained for each stake. Locations of the stakes installed across the glacier shear margin are shown in Fig. S2.

Stake	Latitude (°)	Longitude (°)	$\boldsymbol{v}$ (m a^{-1})	v_x (m a^{-1})	v_y (m a^{-1})	Bearing (°)	Date range	n
HH.	-74.44721	163.49742	45.59±0.56	-8.07±2.31	44.87±0.39	349.02	14-18 Jan	3
GG.	-74.44702	163.49416	63.95±3.45	-2.28±1.01	63.91±3.45	357.62	14-18 Jan	3
FF.	-74.44683	163.49093	72.72±0.18	-1.50±0.40	72.70±0.18	358.73	14-18 Jan	3
EE.	-74.44663	163.48764	77.75±0.20	-2.86±0.52	77.70±0.20	357.82	14-18 Jan	3
DD.	-74.44643	163.48436	81.34±0.62	-0.25±0.45	81.34±0.62	359.27	14-18 Jan	3
CC.	-74.44624	163.48107	81.53±0.83	-2.95±1.06	81.48±0.83	354.96	14-18 Jan	3
O.	-74.44606	163.47784	88.11±0.23	-2.98±0.25	88.06±0.23	357.97	2-18 Jan	9
N.	-74.44596	163.47621	89.33±0.28	-3.13±0.21	89.27±0.28	357.93	2-18 Jan	9
M.	-74.44587	163.47458	89.93±0.23	-2.66±0.21	89.89±0.23	358.21	1-18 Jan	10
L.	-74.44577	163.47295	91.18±0.18	-2.86±0.26	91.13±0.18	358.09	1-18 Jan	10
K.	-74.44568	163.47132	91.68±0.26	-2.63±0.28	91.64±0.26	358.22	2-18 Jan	9
J.	-74.44559	163.46969	92.45±0.37	-2.54±0.23	92.41±0.37	358.33	1-18 Jan	10
I.	-74.44549	163.46806	93.52±0.40	-2.46±0.19	93.49±0.40	358.42	1-18 Jan	10
BB.	-74.44531	163.46480	95.83±0.24	-1.78±0.27	95.82±0.24	358.86	4-18 Jan	5
AA.	-74.44512	163.46154	97.54±0.22	-1.42±0.22	97.53±0.22	359.10	4-18 Jan	5
Z.	-74.44493	163.45828	99.42±0.34	-1.13±0.08	99.41±0.34	359.34	4-18 Jan	5
Y.	-74.44474	163.45498	100.69±0.37	-0.83±0.10	100.69±0.37	359.51	4-18 Jan	5
X.	-74.44455	163.45169	102.56±0.30	-0.54±0.27	102.56±0.30	359.49	5-18 Jan	5
W.	-74.44437	163.44840	104.41±0.70	-0.20±0.22	104.41±0.70	359.63	5-18 Jan	4
V.	-74.44418	163.44512	106.26±0.62	1.97±0.83	106.25±0.62	1.84	5-18 Jan	5
U.	-74.44399	163.44182	107.79±0.40	1.43±0.16	107.78±0.40	0.79	5-18 Jan	5
T.	-74.44380	163.43854	108.91±0.33	1.48±0.16	108.90±0.33	0.75	4-18 Jan	5
S.	-74.44362	163.43527	110.26±0.46	1.76±0.17	110.24±0.46	1.00	4-18 Jan	5
A.	-74.44774	163.47561	87.68±0.16	-4.30±0.30	87.57±0.16	357.08	1-18 Jan	10
B.	-74.44758	163.47409	88.68±0.22	-4.85±0.23	88.54±0.22	356.91	1-18 Jan	10
C.	-74.44726	163.47103	91.03±0.25	-4.79±0.29	90.90±0.25	356.30	1-18 Jan	9
D.	-74.44710	163.46948	91.81±0.30	-4.44±0.23	91.70±0.30	356.55	1-18 Jan	9
E.	-74.44693	163.46793	92.59±0.23	-4.52±0.23	92.48±0.23	357.14	1-18 Jan	10
F.	-74.44677	163.46639	93.44±0.25	-3.93±0.25	93.35±0.25	357.51	1-18 Jan	10
G.	-74.44634	163.46695	93.03±0.27	-3.19±0.14	92.98±0.27	357.99	1-18 Jan	10
H.	-74.44592	163.46750	93.33±0.22	-3.12±0.22	93.28±0.22	358.00	1-18 Jan	10
P.	-74.44648	163.47727	88.18±0.20	-3.75±0.15	88.10±0.20	357.53	1-18 Jan	10
Q.	-74.44690	163.47672	87.60±0.18	-4.25±0.23	87.49±0.18	357.15	1-18 Jan	10
R.	-74.44732	163.47616	88.01±0.25	-4.84±0.26	87.88±0.25	356.77	1-18 Jan	10

1.3 Total station positioning

A total station is a geodetic surveying instrument consisting of an electronic theodolite integrated with an electronic distance measurement (EDM) instrument. These two instruments are used to measure the slope distance, and horizontal and vertical angles to a target. In our case, the target is a reflector prism attached to a glacier stake drilled into the ice surface. Slope distances and angles are used to calculate 3 dimensional positions in a local coordinate system with its origin at the total station. We use a Trimble M3 total station with a range of 2 km, an angular measurement accuracy of 2" (horizontal and vertical),

Table S2. Ice velocity from the total station surveys. Data in the *'Velocity relative to the total station'* columns are independent of any GNSS observations. Stakes S to O form a 2 km transect across the shear margin. Stakes A to F form a second transect. Velocity components v_x and v_y are computed as the slope of the best linear least squares fit for the displacement in the x (across-flow) or y (along-flow) direction versus time.

Stake	Velocity relative to total station			Scaled velocity (total station observations)		
	v_x (m a^{-1})	v_y (m a^{-1})	$\boldsymbol{v}$ (m a^{-1})	v_x (m a^{-1})	v_y (m a^{-1})	$\boldsymbol{v}$ (m a^{-1})
S	5.14±0.24	20.91±2.14	21.53±2.08	2.47±0.24	110.82±2.14	110.85±2.14
U	4.51±0.24	18.61±1.00	19.15±0.98	1.84±0.24	108.52±1.00	108.54±1.00
W	3.72±0.25	15.27±1.16	15.71±1.12	1.05±0.25	105.18±1.16	105.19±1.16
Y	2.63±0.24	10.31±1.63	10.65±1.58	-0.04±0.24	100.22±1.63	100.22±1.63
AA	2.36±0.17	8.29±0.92	8.62±0.88	-0.31±0.17	98.20±0.92	98.20±0.92
BB	1.87±0.18	5.57±0.46	5.88±0.44	-0.80±0.18	95.48±0.46	95.48±0.46
I	1.44±0.15	3.46±0.17	3.75±0.16	-1.23±0.15	93.37±0.17	93.38±0.17
J	1.38±0.15	2.60±0.14	2.94±0.14	-1.29±0.15	92.51±0.14	92.52±0.14
K	1.24±0.15	1.68±0.12	2.08±0.13	-1.43±0.15	91.59±0.12	91.60±0.12
L	1.14±0.19	0.77±0.11	1.38±0.17	-1.53±0.19	90.68±0.11	90.69±0.11
M	1.07±0.18	0.04±0.19	1.07±0.18	-1.60±0.18	89.95±0.19	89.96±0.19
N	0.96±0.17	-0.82±0.22	-1.27±0.19	-1.71±0.17	89.09±0.22	89.11±0.22
O	0.81±0.18	-1.95±0.33	-2.12±0.30	-1.86±0.18	87.96±0.33	87.98±0.33
A	-1.36±0.24	-2.37±0.23	-2.73±0.24	-4.03±0.24	87.54±0.23	87.63±0.23
B	-1.15±0.19	-1.37±0.14	-1.79±0.17	-3.82±0.19	88.54±0.14	88.62±0.14
C	-0.68±0.21	0.45±0.14	0.81±0.19	-3.35±0.21	89.46±0.14	89.52±0.14
D	-0.58±0.22	1.37±0.12	1.49±0.14	-3.25±0.22	91.28±0.12	91.34±0.12
E	-0.29±0.19	2.15±0.15	2.17±0.15	-2.96±0.19	92.06±0.15	92.11±0.15
F	-0.05±0.20	2.97±0.18	2.97±0.18	-2.72±0.20	92.88±0.18	92.92±0.18
R	-0.75±0.16	-2.15±0.39	-2.28±0.37	-3.42±0.16	87.76±0.39	87.83±0.39

and distance accuracy of $\sigma = \pm$ (2+2 ppm $\times$ D) mm[1] (−10 °C to +40 °C) according to instrument specifications (Trimble, 2005). The true accuracy and precision achieved depends on the operator and the local environmental and atmospheric conditions. Repeated measurements at the field site indicate an optimal precision of $1\sigma = 0.46$ mm for slope-distance observations and $1\sigma = 0.49$ mm for horizontal distance observations (D = 200 m). The decline in precision with increasing distance between the total station and target is $1\sigma = 0.46$ mm (D = 200 m) to $1\sigma = 0.72$ mm (D = 1200 m).

1.3.1 Across-flow deformation

Total station positioning is used to resolve mm-scale tidal deflections and deformation of the ice surface that are undetectable with GNSS positioning. Total station observations of prisms installed along the across-flow transect are repeated at 1–2 hour intervals over four diurnal tidal cycles. Observed changes in slope distance are due to along-surface compression and extension resulting from bending stresses. Length changes are used to calculate strain associated with tidal forcing at diurnal and semidiurnal frequencies over two distances, 203 m and 1200 m. This experiment was conducted during the medium tidal range

[1] 1σ of the measured distance is commonly presented by total station manufacturers in the form $\sigma_D = A + B \cdot D$ where A is the absolute accuracy of the EDM in millimetres (a constant), B is an atmosphere-related scale error and is provided in parts per million (ppm) and D is the measured distance in kilometres. B is proportional to the measured distance D (Trimble, 2005; Shih, 2013) This yields a typical accuracy of 1 to 2 mm.

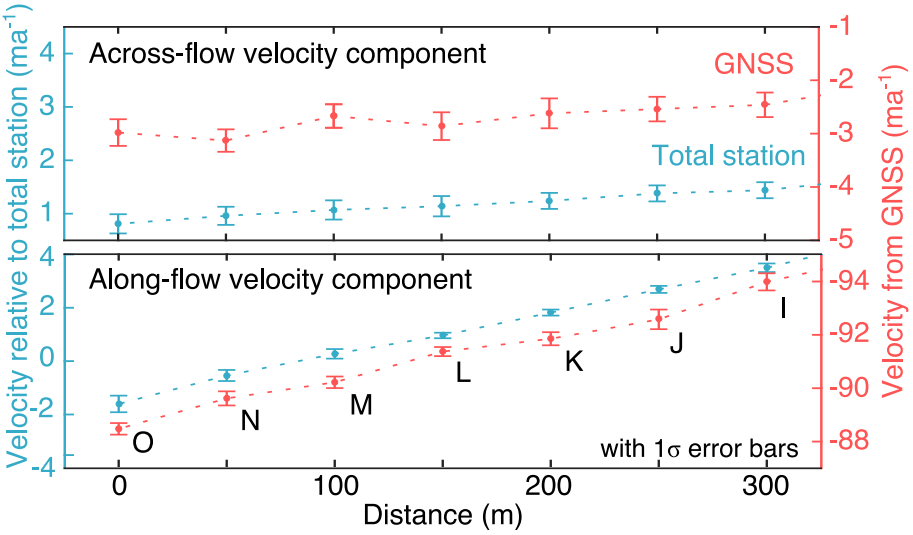

Figure S3. The velocity gradient within a 300 m section of Priestley Glacier's shear margin, inferred from total station and GNSS positioning. Total station positioning provides narrower error bounds and a smoother velocity gradient. The two quantities are plotted on different axes because the total station observations resolve the velocity gradient while GNSS observations resolve the absolute velocity. Converting the total station relative velocities to absolute velocities is possible but introduces an additional error. Locations of glacier stakes O to I are shown in Fig. S2.

observed on the 14th and 15th January, and the neap tide (minimum tidal range) on the 16th and 17th January. The time series of slope-distance changes is presented in Fig. 6.

1.3.2 Total station–derived stake velocity

The network of survey stakes is resurveyed using total station positioning every 1-2 days. These ice displacement observations are presented as the mean velocity for the time period 1-18 January, 2020 (Table S2). Measured stakes are indicated in Fig. S2. Due to the undulating glacier surface topography, it is not possible for all survey stakes to be in the line of sight of the total station.

Total station positioning typically involves the use of fixed reference points to infer the position of the total station, but lack of access to the glacier margin due to crevasses and meltwater ponds prevented the installation of surveying prisms on stationary ground. In lieu of fixed reference points, the continuous GNSS receiver (installed a distance of 4 m from the total station) is used to establish the initial position and displacement of the total station, and distant, distinctive mountain peaks are used to determine the orientation of the coordinate system for the total station observations. Even without a GNSS receiver to establish initial position, total station positioning without fixed reference points still allows the relative velocities of the glacier stakes (and therefore the strain rates) to be inferred. GNSS positioning is also used to determine the absolute position of the total station, however, this introduces an additional error source into the error propagation. Propagated errors in velocity and strain rate associated with the total station and GNSS positioning techniques are compared (Fig. S3). Surveys of 25 of the glacier stakes in the array were conducted on the 1st, 3rd, 5th, 6th, 7th, 8th, 10th, 12th, 16th and 17th of January, 2020. Seven prisms were permanently fixed onto stakes S, U, W, Y, AA, BB, and M, and an 8th prism was transported around the stake network by a team member. Stakes S, U and W (nearest the glacier centre) had permanently installed triple prisms.

1.4 Strain rates and stresses

Deformation in the shear margin is determined from gradients in the GNSS or total station–observed velocity field using the software SSPX (Cardozo and Allmendinger, 2009). The quantity of interest is the strain rate tensor, the symmetrical part of the velocity gradient tensor. Best-fit strain rates are computed for clusters of three or more ice velocity stakes and the relevant equations are detailed here.

For homogeneous deformation, the relationship between velocity vectors and initial positions can be described

$$\boldsymbol{v}_i = \boldsymbol{t}_i + \frac{\partial \boldsymbol{v}_i}{\partial x_j} x_j = \boldsymbol{t}_i + \boldsymbol{D}_{ij} x_j \tag{S3}$$

where $\boldsymbol{v}_i$ is the GNSS-derived velocity vector, $\boldsymbol{t}_i$ corresponds to the velocity of a point at the coordinate system origin (a constant of integration), x_j is the initial position of the GNSS station, and $\boldsymbol{D}_{ij}$ is the asymmetric velocity gradient tensor. The velocity gradient tensor is calculated for the centroid of each glacier stake configuration following Allmendinger et al. (2007, 2009) and Cardozo and Allmendinger (2009). A system of linear equations for each stake configuration is solved for six unknowns in 2D: the four components of $\boldsymbol{D}_{ij}$ and the two components of $\boldsymbol{t}_i$:

$$\begin{bmatrix} {}^1v_1 \\ {}^1v_2 \\ {}^2v_1 \\ {}^2v_2 \\ \dots \\ \dots \\ {}^nv_1 \\ {}^nv_2 \end{bmatrix} = \begin{bmatrix} 1 & 0 & {}^1x_1 & {}^1x_2 & 0 & 0 \\ 0 & 1 & 0 & 0 & {}^1x_1 & {}^1x_2 \\ 1 & 0 & {}^2x_1 & {}^2x_2 & 0 & 0 \\ 0 & 1 & 0 & 0 & {}^2x_1 & {}^2x_2 \\ \dots & \dots & \dots & \dots & \dots & \dots \\ \dots & \dots & \dots & \dots & \dots & \dots \\ 1 & 0 & {}^nx_1 & {}^nx_2 & 0 & 0 \\ 0 & 1 & 0 & 0 & {}^nx_1 & {}^nx_2 \end{bmatrix} \begin{bmatrix} t_1 \\ t_2 \\ D_{11} \\ D_{12} \\ D_{21} \\ D_{22} \end{bmatrix} \tag{S4}$$

where n is the number of glacier stakes used in the strain rate calculation ($n \geq 3$). The equations are solved using a standard least squares solution. A minimum of three stations are required to solve the system of equations. When more than three stations are used, the additional information is used to assess the uncertainties of the best fit strain rates. The velocity gradient tensor $\boldsymbol{D}$ is separated into the strain rate tensor $\dot{\boldsymbol{\epsilon}}_{ij}$ and the rotation rate tensor $\dot{\boldsymbol{\omega}}_{ij}$

$$\boldsymbol{D}_{ij} = \dot{\boldsymbol{\epsilon}}_{ij} + \dot{\boldsymbol{\omega}}_{ij}. \tag{S5}$$

The glaciological effective stress τ_e is the second invariant of the deviatoric stress tensor $\boldsymbol{\tau}_{ij}$ (Cuffey and Paterson, 2010, pg. 59)

$$\tau_e^2 = \frac{1}{2} \boldsymbol{\tau}_{ij} \boldsymbol{\tau}_{ij}. \tag{S6}$$

The octahedral shear stress, a commonly used quantity in geosciences, is $\sqrt{2/3}\tau_e$.

The deviatoric stress tensor $\boldsymbol{\tau}_{ij}$ is computed using the inverse form of the generalised Glen's law

$$\boldsymbol{\tau}_{ij} = A^{-(1/n)} \dot{\boldsymbol{\epsilon}}_e^{(1-n)/n} \dot{\boldsymbol{\epsilon}}_{ij} \tag{S7}$$

where A is a temperature dependent rate factor and n is the flow law exponent ($n = 3$). Values of A corresponding to ice temperatures of -10 °C and -20 °C (Cuffey and Paterson, 2010, pg. 75) are used to calculate effective stresses from strain rates at two different distances from the glacier margin (Table S3).

The ice temperature measured at a depth of 50 m is close to -20 °C (Thomas et al., 2021), thus a simple depth-averaged temperature is likely to be close to -10 °C. The effective strain rate $\dot{\epsilon}_e$ is the second invariant of the strain rate tensor $\dot{\epsilon}_{ij}$

$$\dot{\epsilon}_e^2 = \frac{1}{2}\dot{\epsilon}_{ij}\dot{\epsilon}_{ij}. \tag{S8}$$

Table S3. The Glen's flow law parameters and strain rates used in the effective stress calculation (Eq. S7).

Location	Temperature (°C)	A (Pa^{-3} s^{-1})	n -	τ_e (kPa)	$\dot{\epsilon}_{xx}$ (a^{-1})	$\dot{\epsilon}_{yy}$ (a^{-1})	$\dot{\epsilon}_{xy}$ (a^{-1})
500 m from margin	-20	1.2×10^{-25}	3	233	0.0015	-0.0078	0.0476
	-10	3.5×10^{-25}		163			
GNSS station	-20	1.2×10^{-25}	3	112	0.0032	-0.0030	0.0043
	-10	3.5×10^{-25}		78			

1.4.1 GNSS–observed strain rates within the shear margin

Table S4. Strain triangles in the table are ordered from glacier-left to glacier-right across the shear margin. $\dot{\epsilon}_{xx}$, $\dot{\epsilon}_{yy}$ and $\dot{\epsilon}_{xy}$ are components of the strain rate tensor $\dot{\boldsymbol{\epsilon}}_{ij}$, $\dot{w}$ is the rotation rate, $\dot{\epsilon}_{max}$ and $\dot{\epsilon}_{min}$ are the maximum and minimum principal strain rates, θ is the direction of the principal strain axes, and γ is the maximum shear strain magnitude. The reference frame is the Polar Stereographic Coordinate System and the y-axis is oriented in the along-flow direction for stakes S to Y (ice flow within the shear margin diverges at this location (Fig. S1, Table S1). Negative strain rates indicate compression and positive strain rates indicate extension. Velocity vector components used in the strain rate calculations are from Table S1. Velocities are computed from ten GNSS surveys of the glacier stakes conducted between January 1 to 18, 2020. Stake combinations presented here are chosen to form a triangle as close to equilateral as possible.

Stake triangle	$\dot{\epsilon}_{xx}$ (a^{-1})	$\dot{\epsilon}_{yy}$ (a^{-1})	$\dot{\epsilon}_{xy}$ (a^{-1})	$\dot{w}$ ($^\circ$ a^{-1})	$\dot{\epsilon}_{max}$ (a^{-1})	θ ($^\circ$)	$\dot{\epsilon}_{min}$ (a^{-1})	θ ($^\circ$)	γ (a^{-1})
O, A, margin	0.0019	-0.0080	0.0483	-3.15±0.09	0.0445±0.0038	47.92±0.71	-0.0530±0.0006	137.92±0.71	0.0982±0.0042
GG, DD, A.	0.0104	-0.0293	0.0151	-2.49±0.40	0.0153±0.0278	71.37±16.69	-0.0350±0.0073	161.37±16.69	0.0509±0.0196
A, O, DD.	-0.0125	-0.0042	0.0138	-1.13±0.08	0.0061±0.0089	36.67±4.03	-0.0231±0.0008	126.67±4.03	0.0029±0.0096
O, R, M	0.0042	-0.0021	0.0029	-0.88±0.05	0.0053±0.0103	69.00±10.58	-0.0032±0.0002	159.00±10.58	0.0085±0.0100
R, C, M	0.0038	-0.0008	0.0037	-0.95±0.03	0.0058±0.0083	60.98±4.97	-0.0029±0.0003	150.98±4.97	0.0087±0.0079
C, J, M	0.0019	-0.0003	0.0022	-0.83±0.06	0.0034±0.0086	54.72±5.42	-0.0012±0.0008	144.72±5.42	0.0046±0.0093
J, F, C	0.0048	-0.0001	0.0028	-0.77±0.03	0.0061±0.0088	65.39±10.73	-0.0012±0.0014	155.39±10.73	0.0073±0.0074
J, F, BB	0.0062	-0.0023	0.0058	-0.97±0.05	0.0090±0.0089	63.25±7.05	-0.0055±0.0003	153.25±7.05	0.0143±0.0084

1.4.2 Total station–observed strain rates within the shear margin

Table S5. Strain triangles in the table are ordered from glacier-left to glacier-right across the shear margin. Negative strain rates indicate compression and positive strain rates indicate extension. The velocity components used to compute strain rates were inferred from six total station surveys of glacier stake position between January 1 to 18, 2020.

Stake triangle	$\dot{\epsilon}_{xx}$ (a^{-1})	$\dot{\epsilon}_{yy}$ (a^{-1})	$\dot{\epsilon}_{xy}$ (a^{-1})	$\dot{w}$ ($^\circ$ a^{-1})	$\dot{\epsilon}_{max}$ (a^{-1})	θ ($^\circ$)	$\dot{\epsilon}_{min}$ (a^{-1})	θ ($^\circ$)	γ (a^{-1})
O, R, M	0.0035	-0.0023	0.0046	-0.87±0.12	0.0061±0.0104	61.05±9.75	-0.0049±0.0012	151.05±9.75	0.0110±0.0091
R, C, M	0.0032	-0.0067	0.0011	-0.68±0.09	0.0033±0.0056	83.69±16.78	-0.0069±0.0008	173.69±16.78	0.0102±0.0047
C, J, M	0.0030	-0.0082	0.0034	-0.81±0.01	0.0040±0.0048	74.25±7.26	-0.0092±0.0004	174.25±7.26	0.0132±0.0044
J, F, C	0.0035	-0.0058	0.0058	-0.93±0.01	0.0063±0.0059	64.24±3.11	-0.0086±0.0003	154.24±3.11	0.0149±0.0055
J, F, BB	0.0043	-0.0050	0.0046	-0.88±0.10	0.0062±0.0072	67.56±9.68	-0.0069±0.0005	157.56±9.68	0.0132±0.0077

2 CATS2008 MODEL DOMAIN

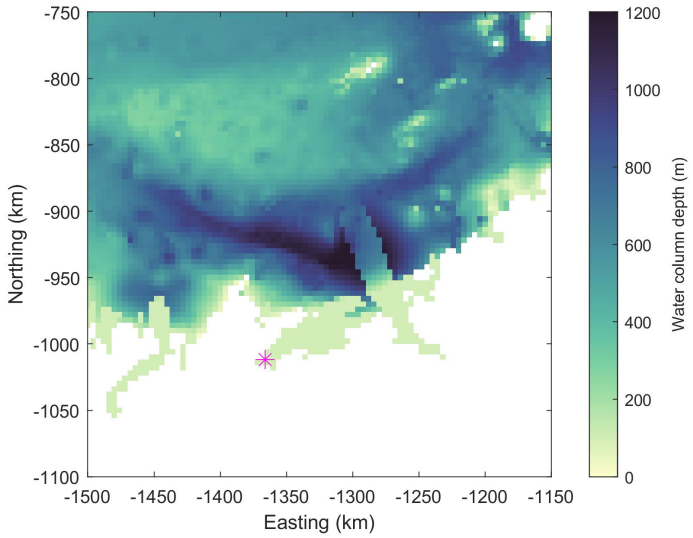

Figure S4. The CATS2008 Terra Nova Bay model domain and water column depth (m). The pink star is the Priestley Glacier field site, located at the edge of the domain.

3 ICE FLEXURE MODEL

3.1 Model geometry

The model equations are solved on an unstructured, triangular, finite element mesh generated using the open source software Gmsh (Geuzaine and Remacle, 2009). Element size ranges from 8 m at the lateral margins and 10 m at the upper/lower boundaries of the ice layer, to 30 m within the model domain centre (Fig. S5). All together, the mesh has 40000 elements.

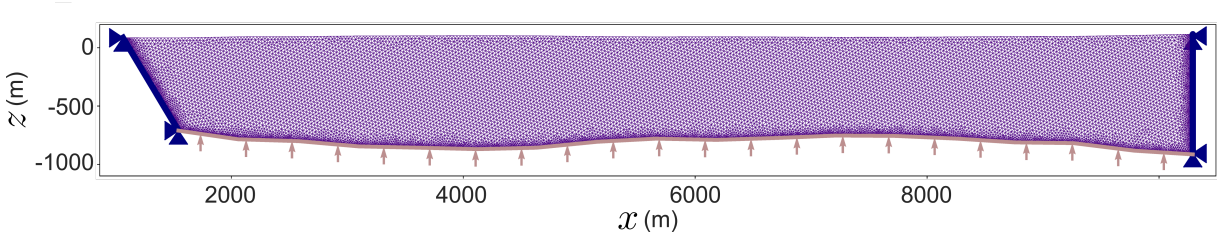

Figure S5. The finite-element mesh used for the elastic bending model. Boundaries are from the MEaSUREs BedMachine Antarctica, Version 2 dataset (Morlighem et al., 2020) and represent an across-flow cross-section of Priestley Glacier. The location of the cross section is indicated in Fig. 1a.

3.2 Boundary condition assumption of zero velocity at the margins

Setting the left-side boundary condition for the model requires an assumption about the connection between the ice and valley sidewall. If some or all of the boundary is fixed, horizontal velocity should equal zero at the glacier edge. Crevasses and meltwater ponds prevented access to the glacier edge, however, the boundary velocity can be estimated using the shape of the observed velocity profile (Figs. S6 and S7).

The best power-law fit between the velocity magnitude and a normalised distance from the glacier centre $\left(1-\frac{x}{X}\right)^n$ (Eq. S9) is for $n = 6$ and the sidewall intercept is 19.3 m a$^{-1}\pm$ 21.4 m a^{-1} (Fig. S6). The fit is not well constrained near the sidewall, more data are needed to improve the velocity estimate, and as it is, the fit suggests spatially varying ice properties to generate the steepest part of the curve.

The transverse velocity profile can be estimated using the analytical solution to the momentum balance for negligible longitudinal stress gradients (Cuffey and Paterson, 2010, pg. 339)

$$v(x) = \frac{2A}{n+1}\left[\rho g \alpha - \frac{\tau_b}{H}\right]^n X^{n+1}\left[1-\left[1-\frac{x}{X}\right]^{n+1}\right] \tag{S9}$$

where v is the depth-averaged ice velocity magnitude, n is the flow law exponent, A is the rate parameter, ρ is the ice density, g is gravitational acceleration, α is the surface slope, τ_b is the basal drag, H is the ice thickness, X is half the width of the glacier and x is the distance from the margin ($x = 0$ at the margin). The model cross-section is freely floating and $\tau_b = 0$. The data do not fit any single curve (Fig. S7), but instead suggest spatially variable ice properties: softer near the margin and stiffer away from the margin.

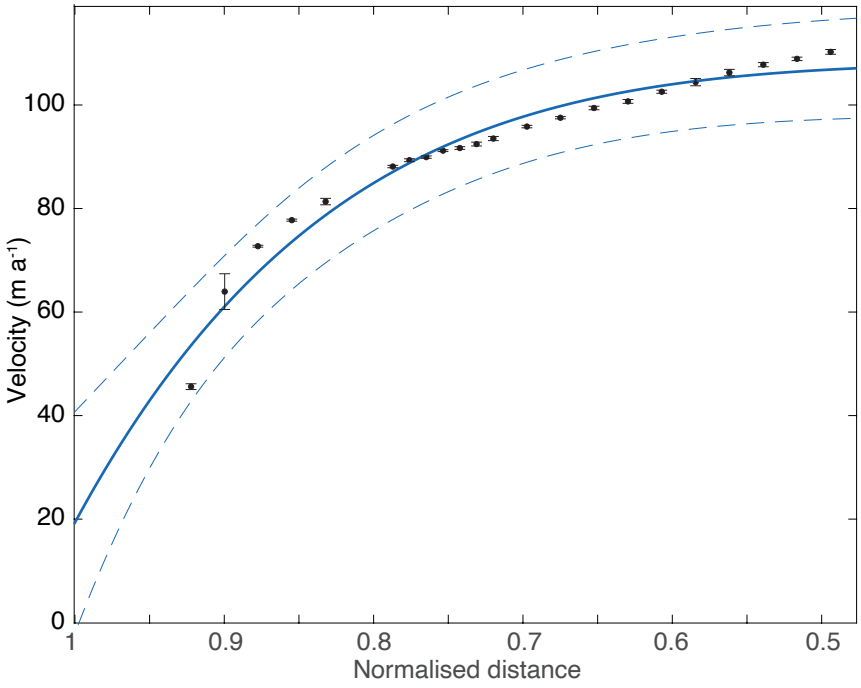

Figure S6. Best power-law fit to the observed velocity magnitude used to estimate velocity at the glacier edge, computed using the MATLAB 2022a Curve Fitting Toolbox functions such that $f(x) = -88.8x^6 + 108.1$. The R^2 value is 0.96 and 99% prediction bounds are shown.

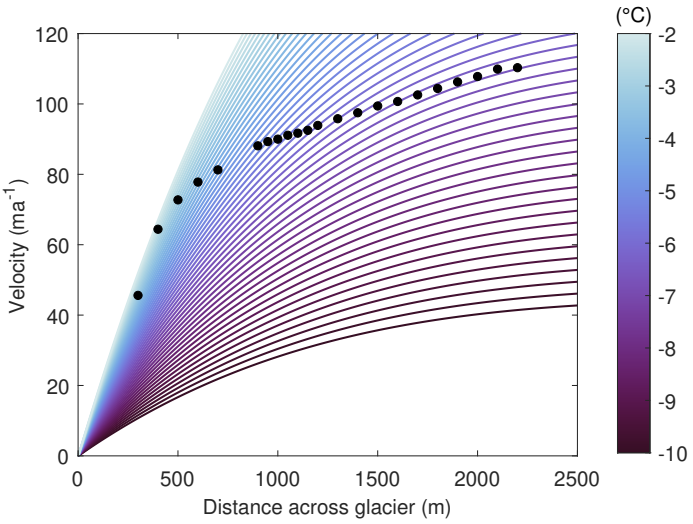

Figure S7. Theoretical transverse velocity profiles and the GNSS velocity observations. A ranges from 3.5×10^{-25} to 1.7×10^{-24} Pa^{-3} s^{-1}, corresponding to an ice temperature range of -10 to -2 °C. The glacier width is 9 km, the surface slope is 3×10^{-3} and n = 3.

3.3 Tide forcing applied to the reference model M1

Table S6. Root mean square error (RMSE) (cm) between observed and modelled horizontal position for a range of tide forcings. The tide forcing refers to the scaling of the CATS2008 tide prediction.

	Tide forcing				
E (GPa)	$\times1$	$\times0.75$	$\times0.7$	0.6	$\times0.5$
1.5	1.12	0.76	0.70	0.60	**0.55**
2	0.91	0.64	0.61	0.56	**0.55**
2.5	0.78	0.58	0.56	**0.55**	0.56
3	0.68	**0.55**	**0.55**	**0.55**	0.59
3.5	0.62	**0.55**	**0.55**	0.57	0.61
4	0.58	**0.55**	0.56	0.59	0.63
4.5	0.56	0.56	0.57	0.61	0.65
5	**0.55**	0.57	0.59	0.62	0.67
5.5	**0.55**	0.59	0.60	0.64	0.69
6	**0.55**	0.60	0.62	0.66	0.71

Table S7. RMSE (cm) between observed and modelled vertical position for a range of tide forcings.

	Tide forcing				
E (GPa)	$\times 1$	$\times 0.75$	$\times 0.7$	0.6	$\times 0.5$
1.5	1.89	1.41	1.33	1.19	1.12
2	1.60	1.25	1.19	1.11	1.07
2.5	1.41	1.15	1.12	1.07	**1.06**
3	1.28	1.10	1.08	**1.06**	**1.06**
3.5	1.20	1.08	1.07	**1.06**	1.07
4	1.14	**1.06**	**1.06**	1.07	1.08
4.5	1.11	**1.06**	**1.06**	1.08	1.09
5	1.08	**1.06**	1.07	1.09	1.10
5.5	1.07	1.07	1.08	1.11	1.11
6	**1.06**	1.08	1.09	1.12	1.12

3.4 Model results: downward bending

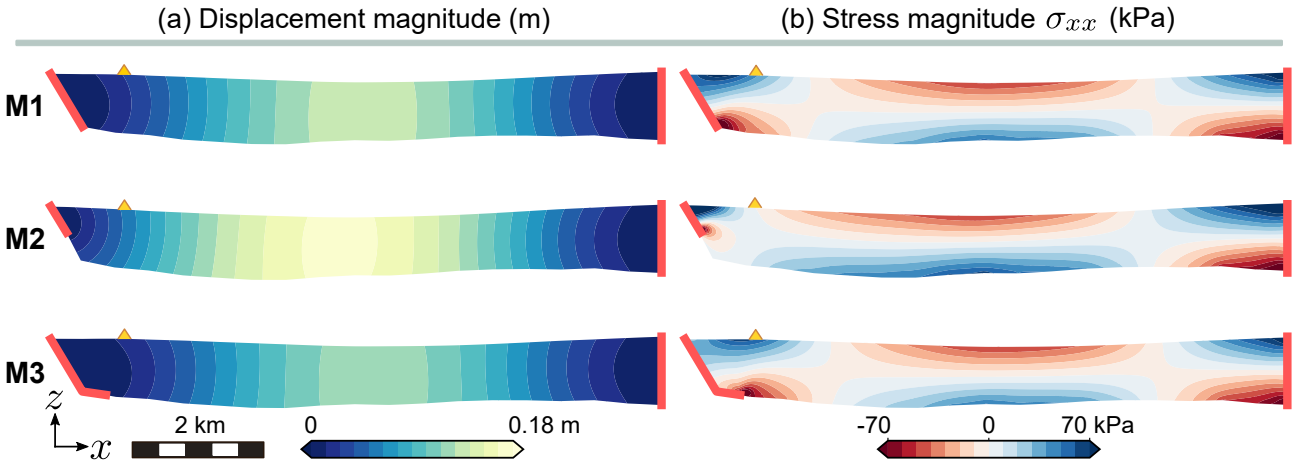

Figure S8. Downward bending of the ice layer for three different left lateral boundary conditions. M1 is the reference model, M2 has a partially fixed left boundary and M3 represents additional grounding on the seafloor. The first column shows the displacement magnitude and the second column is the transverse (across-flow) component of the stress tensor. Negative stresses are compressive and positive stresses are tensile. The tide forcing is -37 cm, representing the scaled spring low tide. All experiments have a uniform Young's modulus of $E = 4$ GPa. Opposite upward bending is shown in Fig. 8.

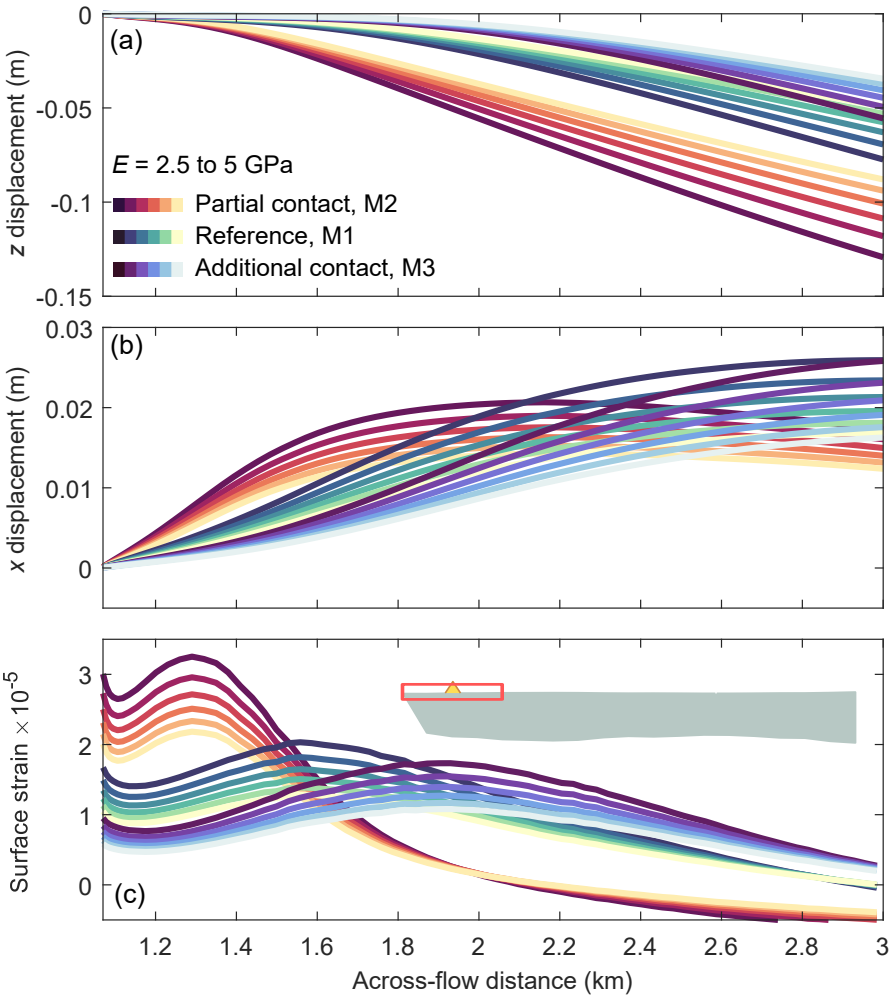

Figure S9. Panel (a) is the vertical component z of the ice surface displacement for each of the three margin boundary conditions and a range of Young's modulus values ($E = 2.5$ to 5 GPa, dark to light shading, respectively). Panel (b) is the horizontal component x of the ice surface displacement, with positive displacements indicating motion away from the margin. Panel (c) is the surface strain (engineering strain) computed for each model element at the ice surface. The tide forcing applied to generate the downward deflection in this example is the spring low tide (-37 cm). The red inset box indicates the section of the glacier surface shown in each plot.

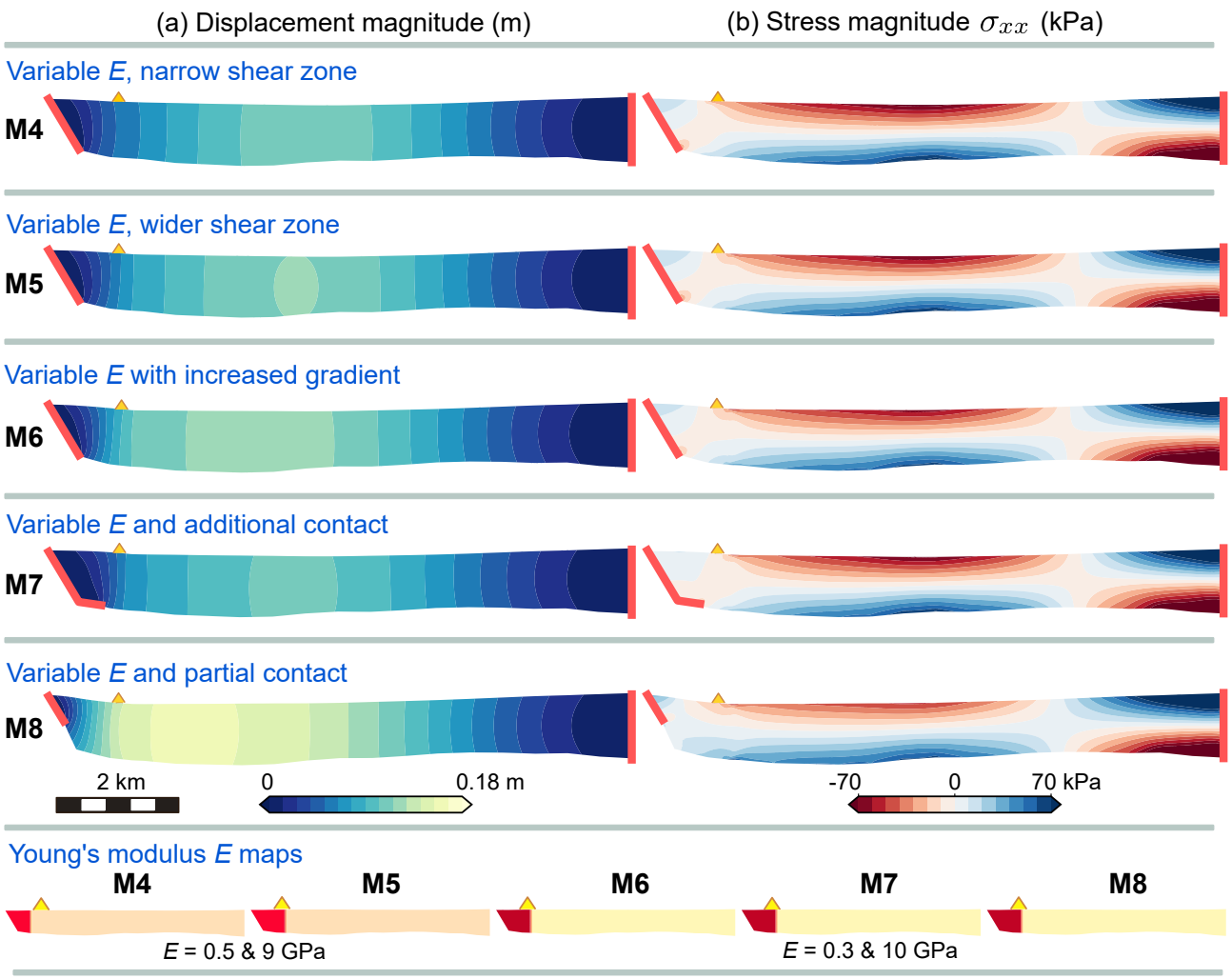

Figure S10. Downward deflection of the ice layer for five experiments with spatially variable E across the shear margin. The first column shows the displacement magnitude and the second column is the transverse (across-flow) component of the stress tensor. Negative stresses are compressive and positive stresses are tensile.

REFERENCES

Allmendinger, R. W., Loveless, J. P., Pritchard, M. E., and Meade, B. (2009). From decades to epochs: Spanning the gap between geodesy and structural geology of active mountain belts. *Journal of Structural Geology* 31, 1409–1422. doi:10.1016/J.JSG.2009.08.008

Allmendinger, R. W., Reilinger, R., and Loveless, J. (2007). Strain and rotation rate from GPS in Tibet, Anatolia, and the Altiplano. *Tectonics* 26, 3013. doi:10.1029/2006TC002030

Cardozo, N. and Allmendinger, R. W. (2009). SSPX: A program to compute strain from displacement/velocity data. *Computers and Geosciences* 35, 1343–1357. doi:10.1016/j.cageo.2008.05.008

Cuffey, K. M. and Paterson, W. S. B. (2010). *The Physics of Glaciers* (Burlington, MA: Elsevier), 4th edn.

Geuzaine, C. and Remacle, J. F. (2009). Gmsh: A 3-D finite element mesh generator with built-in pre- and post-processing facilities. *International Journal for Numerical Methods in Engineering* 79, 1309–1331. doi:10.1002/NME.2579

Howat, I. M., Porter, C., Smith, B. E., Noh, M.-J., and Morin, P. (2019). The Reference Elevation Model of Antarctica. *The Cryosphere* 13, 665–674. doi:10.5194/tc-13-665-2019

Morlighem, M., Rignot, E., Binder, T., Blankenship, D., Drews, R., Eagles, G., et al. (2020). Deep glacial troughs and stabilizing ridges unveiled beneath the margins of the Antarctic ice sheet. *Nature Geoscience* 13, 132–137. doi:10.1038/s41561-019-0510-8

Shih, P. T.-Y. (2013). On accuracy specifications of electronic distance meter. *Survey Review* 45, 281–284. doi:10.1179/1752270612Y.0000000035

Taylor, J. R. (1997). *An Introduction to Error Analysis: the Study of Uncertainties in Physical Measurements* (New York, NY: University Science Books)

Thomas, R. E., Negrini, M., Prior, D. J., Mulvaney, R., Still, H., Bowman, M. H., et al. (2021). Microstructure and Crystallographic Preferred Orientations of an Azimuthally Oriented Ice Core from a Lateral Shear Margin: Priestley Glacier, Antarctica. *Frontiers in Earth Science* 9, 1084. doi:10.3389/feart.2021.702213

Trimble (2005). *Trimble M3 Total Station*. Tech. rep. doi:http://trl.trimble.com/docushare/dsweb/Get/Document-262358/022543-155J_TrimbleM3_DS_0414_LR.pdf